

# **A Modeling Technique and Representation of Failure in the Analysis of Triaxial Braided Carbon Fiber Composites**

Justin D. Littell and Wieslaw K. Binienda  
University of Akron  
Akron, Ohio 44325

Robert K. Goldberg and Gary D. Roberts  
National Aeronautics and Space Administration  
Glenn Research Center  
Cleveland, Ohio 44135

## **Abstract**

Quasi-static tests have been performed on triaxially braided carbon fiber composite materials with large unit cell sizes. The effects of different fibers and matrix materials on the failure mode were investigated. Simulations of the tests have been performed using the transient dynamic finite element code, LS-DYNA. However, the wide range of failure modes observed for the triaxial braided carbon fiber composites during tests could not be simulated using composite material models currently available within LS-DYNA. A macroscopic approach has been developed that provides better simulation of the material response in these materials. This approach uses full-field optical measurement techniques to measure local failures during quasi-static testing. Information from these experiments is then used along with the current material models available in LS-DYNA to simulate the influence of the braided architecture on the failure process. This method uses two-dimensional shell elements with integration points through the thickness of the elements to represent the different layers of braid along with a new analytical method for the import of material stiffness and failure data directly. The present method is being used to examine the effect of material properties on the failure process. The experimental approaches used to obtain the required data will be described, and preliminary results of the numerical analysis will be presented.

## **Introduction**

The analysis of laminated composite materials within a finite element code requires the input of unidirectional engineering properties of the composite lamina such as Young's modulus and Poisson's ratio in various coordinate directions. The fiber orientations of each of the plies in the laminate are provided, and Classical Laminated Plate Theory (CLPT) (ref. 1) is then applied within the finite element code to compute the effective laminate stiffness and deformation response of the composite based on the ply material data and fiber orientations. The unidirectional properties of the composite ply can be measured from testing and input directly into the code, or computed based on fiber and matrix constitutive properties using micromechanics methods such as the Rule of Mixtures, the Concentric Cylinders Model (ref. 1), or other techniques. The composite structure is then modeled in most cases using two-dimensional shell elements and in some cases by three-dimensional brick elements.

However, while CLPT works well for traditional unidirectional laminated composites, it cannot be directly used with braided or woven composites because the fibers are interwoven, and a clear distinction cannot be made between each of the individual layers. There has been research to refine traditional CLPT equations to account for the complex braid architecture in woven or braided composites, and an overview of these methods is shown in reference 2; however this topic is still an area of research.

Numerous approaches for modeling composites having nontraditional layers have been developed, and some examples are discussed here. Dano et al. (ref. 3) modeled two-dimensional triaxial braided composite static tensile coupons using beam elements for the carbon fiber and shell elements as the

polymer matrix material. Masters et al. (ref. 4) performed extensive testing on triaxial braided composites and developed two finite element techniques to calculate the stiffness of the composite. The first of these models was called the “diagonal brick model,” which used a brick of resin as the outlining element with bar elements representing the carbon fiber braid.

Similar methods have been developed specifically for woven composites. Donadon et al. (ref. 5) developed a three-dimensional constitutive model based on CLPT for woven laminates, and Huang (ref. 6) developed a “bridging model” for woven composites based on undulations and composite geometry. An approach developed by Ishikawa and Chow (ref. 7) called the “mosaic model” simulated a woven composite by breaking up a unit cell into squares of unidirectional lamina. In this model, laminate properties are found by assembling the unidirectional lamina through application of CLPT. Tabiei and Tanov (ref. 8) have developed a “four cell model” for plain weave composites, which breaks down the unit cell into subcells and develops equations that include the fiber undulation angles.

The approach that has been developed in this paper entails development of a macromechanical model capable of being used in large composite structures. The approach uses methods based on traditional CLPT to analyze the braided composite at the macromechanical level. The equivalent unidirectional ply properties of the composite required for the analysis are obtained by utilizing results from tests on the braided composite. Because the model approximates the braid architecture while also incorporating many of the failure properties of the composite, it accounts for elements of the composite microstructure but only requires the smaller computation time of a macromechanical approach. Finally, the model can be easily modified to account for changes in the braid angle, number of layers, or materials.

## Material Background

A high-strength, standard-modulus fiber (T700S, Toray Industries, Inc.) was used along with a toughened resin (CYCOM PR520, Cytec Industries, Inc.) for this study. The composite material system was fabricated into 2-ft by 2-ft by 0.125-in. composite panels in an enclosed resin transfer molding (RTM) mold by North Coast Composites using braided preforms from A&P Technology. The preform architecture was  $[0^\circ/60^\circ/-60^\circ]$  with 24k tows (“24k” is a designation of the number of fiber filaments in a fiber tow) in the axial ( $0^\circ$ ) direction and 12k tows in the bias ( $60^\circ$  and  $-60^\circ$ ) directions. The number of 24k tows in the axial direction was half that of the 12k tows in the bias directions, so the total fiber volume in each direction was the same. As a result the composite is expected to be quasi-isotropic. The preform was supplied in the form of a braided tube. Three layers of the tube (six total plies) were excised, placed in the RTM mold with  $0^\circ$  (axial) fibers aligned, injected with resin, and cured under conditions specified by the resin manufacturer. The nominal fiber volume was calculated to be 56 percent, and the actual fiber volume was measured by the acid digestion technique on samples from a representative panel for each material system. The fiber volume of the composite panel was measured to be  $55.9 \pm 0.18$  percent. Figure 1 shows an example of the braided material and the size of a unit cell. The unit cell is the smallest repeating volume of the composite where the behavior can be considered to be representative of the composite as a whole. For the analyses conducted in this study, a single unit cell is also divided into four subcells.

Figure 1, left, shows the fiber orientation in a braided preform before molding. Figure 1, upper right, shows a magnification of one unit cell for one layer of braid of the composite. Figure 1, middle right, shows a top view of the three-dimensional model of the braid architecture, and figure 1, lower right, shows a side view of the braid architecture with the subcells identified. Each subcell is simulated as an equivalent laminated composite. Note that due to the braiding scheme present, the fiber layup is different in each of the subcells. As shown by the subcell illustrations in figure 1, middle right, subcell A has a  $-60^\circ$  fiber on top (represented in green), a  $0^\circ$  fiber in the middle (represented by blue), and a  $60^\circ$  fiber on the bottom (represented by red) in each layer. Similarly, subcell B is shown to have only a  $-60^\circ$  fiber over a  $60^\circ$  fiber, and subcell C has a  $60^\circ$  fiber over a  $0^\circ$  fiber on top of a  $-60^\circ$  fiber. Finally, subcell D has a  $60^\circ$  fiber over a  $-60^\circ$  fiber. Therefore, the braid architecture is simulated by the process of dividing up the unit cell into subcells and approximating each subcell as a laminated composite.

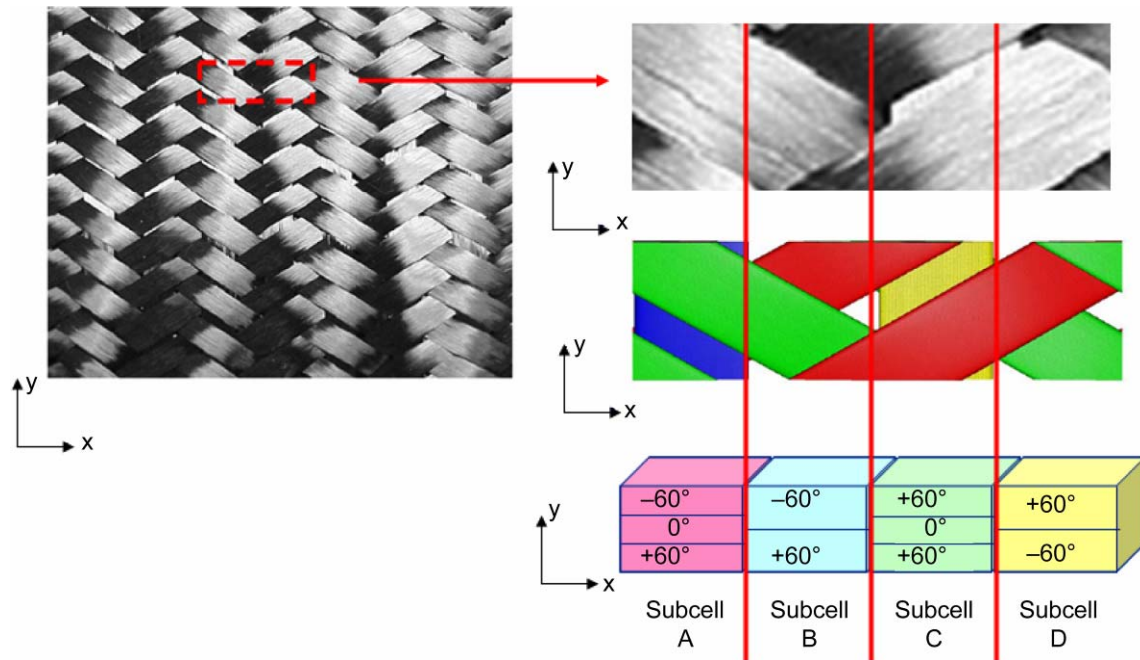


Figure 1.—Triaxial braided composite with unit cell.

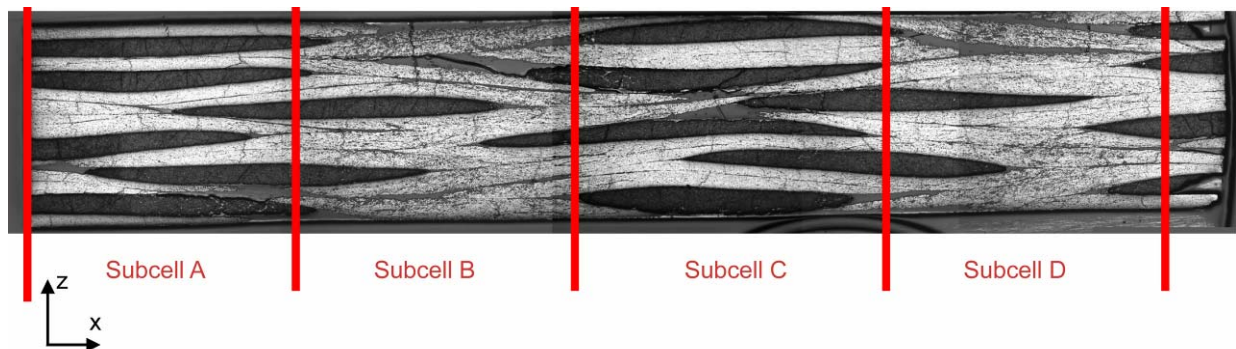


Figure 2.—Side view photomicrographs of triaxial braided composite cross section.

The unit cell with subcell geometries as defined here will be the basis for the modeling technique.

Figure 1 shows the architecture of a single layer of braid in a unit cell. The actual composite panels have six layers of braid (with each layer of braid having multiple layers of fiber tows). Photomicrographs were taken to determine the amount of fiber shifting, or the relative position of the unit cells through the specimen thickness, present in the actual composite panel. Fiber shifting was examined because if it was assumed that all of the subcells would be in the same relative position throughout the thickness, then subcells B and D would be overly weak due to the lack of  $0^\circ$  fibers in these subcells. Also, shifting was included to account for the assumption of quasi-isotropy, in that each of the subcells would have  $0^\circ$ ,  $-60^\circ$ , and  $60^\circ$  fibers.

Figure 2 shows a side view cross-section photomicrograph of an actual composite panel. The dark areas represent the cross sections of the axial fiber bundles, as they are orientated perpendicular to the page, while the white areas represent bias fiber bundles, which are orientated at  $30^\circ$  to the cross-sectional cut. The small areas of grey between the fiber bundles represent resin rich pockets. Subcell designations shown in the figure were picked to represent the subcells for the top layer of braid. Subsequent layers are

shown to have misalignments under the topmost layer, where for example one  $0^\circ$  fiber tow is found directly under another  $0^\circ$  fiber tow. These relative changes in position for subsequent layers through the thickness suggest that subcell shifting is prevalent enough such that it needs to be accounted for in the analytical model. Subcell shifting will be accounted for in an idealized way when modeling the braid geometry. The analysis method will shift the relative location of a unit cell by one subcell for each of the layers through the thickness of the composite.

## **Finite Element Model Development**

The commercial transient dynamic finite element code, LS-DYNA (ref. 9), was used to analyze the triaxial braided composites discussed in this paper. The LS-DYNA code was used because of its applicability to impact simulations, which will be the ultimate goal of this effort and discussed in a future paper.

Both the triaxial braid geometry and the material properties obtained through testing will be incorporated into the model. First, the composite test techniques will be briefly described. Next, the methods for including the composite braid architecture will be discussed, and finally, the methods developed for obtaining the equivalent unidirectional ply properties required for the finite element model from the test data will be presented.

## **Experimental Results**

Tensile, compressive, and shear testing was completed for the T700S fiber/PR520 resin triaxial braided composite material system under consideration, and a full description of the test method can be found in reference 10. Optical measurement techniques were used to capture the full-field surface strain on the composite test specimens. By examining the full-field data, representative material property data for the composite such as effective stress-strain curves were obtained; however, the optical measurement techniques allowed for greater insight into local failure mechanisms occurring in individual fiber bundles or specific layers. One main advantage of this approach is that the optical measurement techniques were also able to capture individual subcell axial and transverse strains on the surface of the specimen, which allowed for the utilization of the strain data in the material model (described later). Figure 3 shows example results obtained from the optical measurement system, with subcell strains highlighted.

## **Development of Braid Geometry**

The idealized geometry to be represented in the computer finite element model is shown in figure 4. The model developed in this report is an extension of techniques first developed by Cheng (ref. 11), which are being modified because reference 11 failed to include the fiber shifting phenomena observed and described in the previous section.

In the LS-DYNA model, each subcell is modeled as a discrete entity, called a Part (\*PART...). Each Part has its own corresponding Section (\*SECTION...), which will define the braid geometry, and Material (\*MAT...), which will incorporate the equivalent unidirectional ply properties obtained from the test data. All subcells were modeled as shell elements (\*SECTION\_SHELL) since the length and width of the composite structures being examined are much greater than the thickness. Each section card contains properties such as element thickness, which represents the thickness of the composite specimen; number of integration layers, which defines the number of fiber layers through the cross section; and integration layer orientation, which describes the angle of the fiber at each particular layer. Thus, the section card in each of the subcells includes 15 integration points that represent the 15 layers of fibers through the thickness of the composite. Finally, separate integration cards (\*INTEGRATION...) were used for each subcell. This card is called out by the individual subcell section cards and includes parameters such as individual fiber layer position through the thickness of the section and relative weights for each layer. To simplify the development of the material model, the analysis method assumes each of the 15 fiber layers have the same thickness; thus all of the fiber layers are

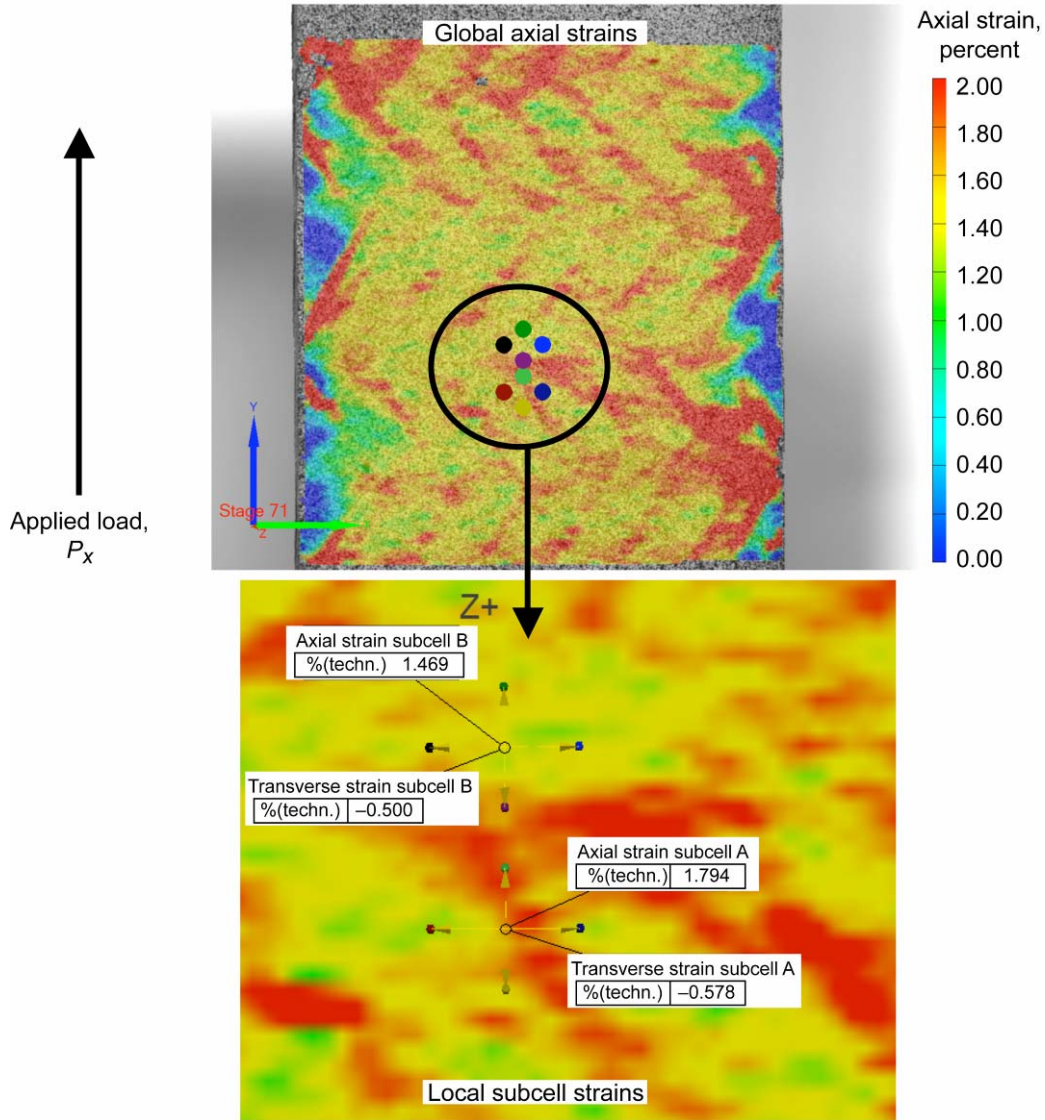


Figure 3.—Optical measurement system example results with subcell strains highlighted.

spaced equally throughout the thickness. To account for the differences in sizes between the 24k axial and 12k bias fiber bundles, the axial layers were weighted twice the amount of the bias layers.

As an example, subcell A (fig. 4) would be modeled as part no. 1, which has a corresponding section no. 1. Section no. 1's integration layers will reflect the braid geometry seen in figure 4. Going from bottom to top in subcell A, the orientation of the fibers are as follows:  $-60^\circ$ ,  $60^\circ$ ,  $60^\circ$ ,  $0^\circ$ ,  $-60^\circ$ ,  $-60^\circ$ ,  $60^\circ$ ,  $-60^\circ$ ,  $0^\circ$ ,  $60^\circ$ ,  $-60^\circ$ ,  $60^\circ$ ,  $60^\circ$ ,  $0^\circ$ ,  $-60^\circ$ . All layers would be equally spaced, and the normalized weights on the axial ( $0^\circ$ ) fibers would be double that of the bias ( $60^\circ$ ) layers.

### Development of Material Property Values

The material model within LS-DYNA that was employed for all of the subcells is a continuum damage mechanics-based orthotropic material model based on a model developed by Matzenmiller et al. (ref. 12). This model is known as \*MAT\_LAMINATED\_COMPOSITE\_FABRIC (Material 58) within LS-DYNA. For the elastic portion of the analysis, which will be described first, the effective

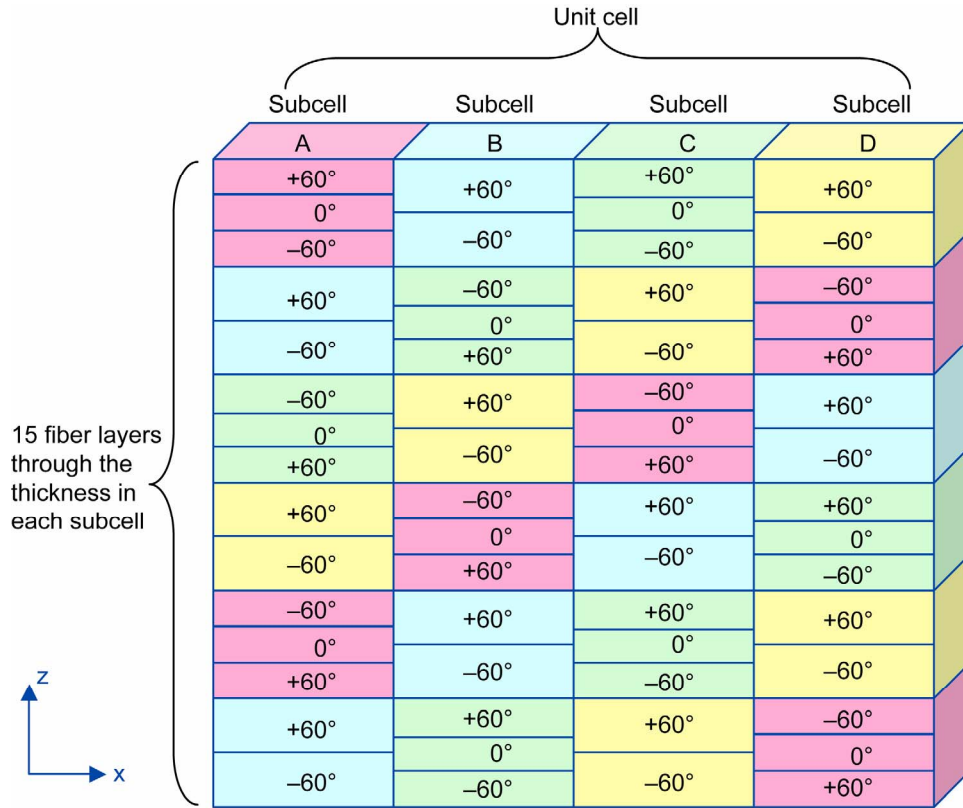


Figure 4.—Cross section of idealized model used for FEM geometry (side view).

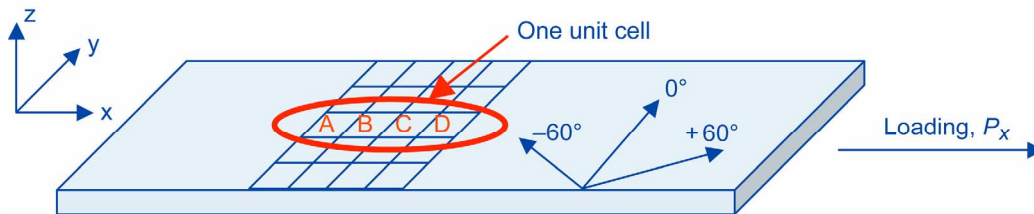


Figure 5.—ASTM D 3039 Transverse tensile test configuration.

unidirectional ply properties, the longitudinal Young's modulus  $E_{11}$ , transverse Young's modulus  $E_{22}$ , transverse Poisson's ratio  $\nu_{21}$ , and axial shear modulus  $G_{12}$ , need to be entered as part of the model input.

The methods for obtaining the effective unidirectional ply level properties ( $E_{11}$ ,  $E_{22}$ ,  $\nu_{21}$ ,  $G_{12}$ ) that are needed for each integration layer in each of the subcells are developed in this section. The key feature of this approach is that the required properties can be backed out from coupon-level test data obtained for the braided composite. As part of this process, the analysis method developed was done in parallel with testing done by Littell et al. (ref. 10). Thus, many of the specimen geometries and boundary conditions utilized for model development are the same as those used in the composite testing. The first step in the model development process involves examining results from a transverse tensile test, in which the specimen geometry was taken from the ASTM D-3039 (ref. 13) standard. In this test, the axial ( $0^\circ$ ) fibers are oriented perpendicular to the applied load,  $P_x$ , as shown in figure 5. To represent the transverse tensile test in the model, the four subcells of the unit cell are orientated parallel to the direction of the load, also shown in figure 5.

By first assuming that all six layers of braid in the specimen carry the same load, the total load is first divided by the number of layers in the composite. Next, it is assumed that all of the unit cells along the width of the specimen carry the same load, so the applied load is divided by the number of unit cells along the width, which gives the total load for each unit cell. By applying this approach the model is developed for the unit cell as shown in figure 1 and is not developed for the shifted geometry as shown in figure 3. A point to note is that the axial load  $N_x$  is taken to be per unit length so it is also divided by the width of each unit cell.

$$N_x = \frac{P_x}{(\#layers * \#unit\ cells * width)} \quad (1)$$

The next step is to partition the load  $N_x$  among each of the subcells in the unit cell. For this process, and for the methods described in the remainder in this section, uniform stress (or load) and uniform strain assumptions that have been applied in micromechanics methods in the past (ref. 14) need to be applied between the subcells. For example, the load  $N_x$  can be assumed to be equal in all of the subcells

$$N_x^A = N_x^B = N_x^C = N_x^D \quad (2)$$

The subscript  $x$  represents the direction of loading (see fig. 5) and the superscript represents the subcell name. Next, the volume average of the load in the  $y$ -direction,  $N_y$ , in each of the subcells is assumed to be equal to 0 since there is no applied load in that direction.

$$(V_f^A * N_y^A) + (V_f^B * N_y^B) + (V_f^C * N_y^C) + (V_f^D * N_y^D) = 0 \quad (3)$$

$V_f$  represents the volume fraction of each subcell compared with the volume of the entire unit cell, and not the fiber volume fraction of the as-fabricated composite. Note that because subcell C will have the same volume fraction as subcell A and subcell D will have the same volume fraction as subcell B, equation (3) can be rewritten.

$$2(V_f^A * N_y^A) + 2(V_f^B * N_y^B) = 0 \quad (4)$$

Next, CLPT is used to relate  $N_x$  and  $N_y$  in each subcell to the to the strains  $\varepsilon$  in the subcell. Although on a local level the laminate orientations in each subcell are not symmetric, on a global level the composite can be assumed to be symmetric, so the assumption is made that the B constitutive matrix normally associated with CLPT can be set equal to zero. Furthermore, on the local level only the in-plane strains are considered, not any moments, so the D matrix normally associated with CLPT is also assumed to be zero. The laminate orientations can be assumed to be balanced, so the A16 and A26 components of the A matrix from CLPT are set equal to zero. To summarize, in-plane normal loads are assumed to be a function of in-plane normal strains, and shear loads are assumed to be a function of shear strains.

$$\begin{bmatrix} N_x^A \\ N_y^A \\ N_{xy}^A \end{bmatrix} = \begin{bmatrix} A11^A & A12^A & 0 \\ A12^A & A22^A & 0 \\ 0 & 0 & A66^A \end{bmatrix} \begin{bmatrix} \varepsilon_x^A \\ \varepsilon_y^A \\ \varepsilon_{xy}^A \end{bmatrix} \quad (5)$$

In equation (5), the superscript  $A$  represents the subcell name. The equation has the same form for subcells B, C, and D. The matrix equation shown in equation (5) above can be expanded to give equations (6) and (7) for subcell A and equations (8) and (9) for subcell B.

$$N_x^A = (A_{11}^A * \varepsilon_x^A) + (A_{12}^A * \varepsilon_y^A) \quad (6)$$

$$N_y^A = (A_{12}^A * \varepsilon_x^A) + (A_{22}^A * \varepsilon_y^A) \quad (7)$$

$$N_x^B = (A_{11}^B * \varepsilon_x^B) + (A_{12}^B * \varepsilon_y^B) \quad (8)$$

$$N_y^B = (A_{12}^B * \varepsilon_x^B) + (A_{22}^B * \varepsilon_y^B) \quad (9)$$

Noting that subcells A and C will both have the same layers of  $0^\circ$  fibers, layers of  $60^\circ$  fibers and layers of  $-60^\circ$  fibers, only subcell A will be examined. Similarly, since subcells B and D will have the same number of  $60^\circ$  and  $-60^\circ$  layers, only subcell B will be examined.

The A matrix from CLPT can be computed in the usual manner:

$$A_{ij} = \sum_k \bar{Q}_{ij} * t_k \quad (10)$$

In equation (10),  $t$  is the thickness of the  $k^{\text{th}}$  layer. The  $A_{ij}$  matrix can be specifically written for subcells A and B.

$$\begin{aligned} A_{11}^A &= \bar{Q}_{11}^{0^\circ} * t + \bar{Q}_{11}^{-60^\circ} * t + \bar{Q}_{11}^{60^\circ} * t \\ A_{12}^A &= \bar{Q}_{12}^{0^\circ} * t + \bar{Q}_{12}^{-60^\circ} * t + \bar{Q}_{12}^{60^\circ} * t \\ A_{22}^A &= \bar{Q}_{22}^{0^\circ} * t + \bar{Q}_{22}^{-60^\circ} * t + \bar{Q}_{22}^{60^\circ} * t \end{aligned} \quad (11)$$

$$\begin{aligned} A_{11}^B &= \bar{Q}_{11}^{-60^\circ} * t + \bar{Q}_{11}^{60^\circ} * t \\ A_{12}^B &= \bar{Q}_{12}^{-60^\circ} * t + \bar{Q}_{12}^{60^\circ} * t \\ A_{22}^B &= \bar{Q}_{22}^{-60^\circ} * t + \bar{Q}_{22}^{60^\circ} * t \end{aligned} \quad (12)$$

In equations (11) and (12), the  $\bar{Q}_{ij}$  terms are the transformed stiffness terms for a unidirectional ply in the structural axis system. Note that a  $\bar{Q}_{ij}$  term for the  $0^\circ$  fiber is not present in subcell B because  $0^\circ$  fibers are not present in this subcell. The  $\bar{Q}_{ij}$  terms can now be decomposed into their representative  $Q$  terms, which represent the stiffnesses for a unidirectional ply in the material axis system in the axial, transverse, and shear directions. In general,

$$\begin{aligned} \bar{Q}_{11} &= m^4 * Q_{11} + n^4 * Q_{22} + 2 * n^2 * m^2 * Q_{12} + 4 * m^2 * n^2 * Q_{66} \\ \bar{Q}_{12} &= m^2 * n^2 * Q_{11} + m^2 * n^2 * Q_{22} + (m^4 + n^4) * Q_{12} - 4 * m^2 * n^2 * Q_{66} \\ \bar{Q}_{22} &= n^4 * Q_{11} + m^4 * Q_{22} + 2 * n^2 * m^2 * Q_{12} + 4 * m^2 * n^2 * Q_{66} \end{aligned} \quad (13)$$

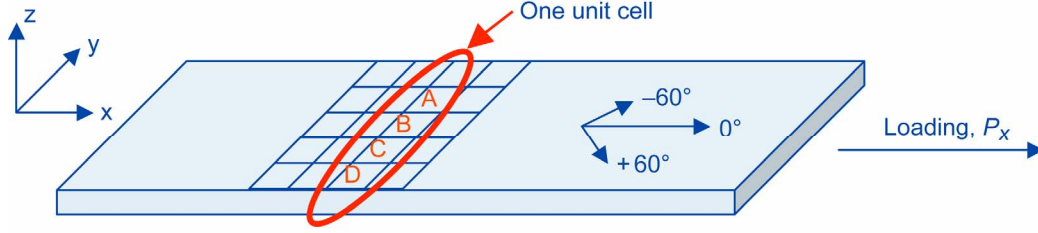


Figure 6.—Axial tension test schematic.

In equation (13),  $m$  is the cosine of the braid angle and  $n$  is the sine of the braid angle. Thus equation (13) can be substituted into equations (11) and (12) noting that the values for  $m$  and  $n$  will change for the different bias directions.

There are now six unknowns in the equations derived above— $Q_{11}$ ,  $Q_{12}$ ,  $Q_{22}$ ,  $Q_{66}$ ,  $N_y^a$ ,  $N_y^b$ —and only five equations—equations (4) and (6) to (9). An advantage to using an optical measurement system is that it allows for the strains in both the axial and transverse directions to be directly measured for each of the subcells and used directly in equations (6) to (9).

However, the system needs another equation to be solvable. This equation will be found from the modeling of an axial tensile test using the same ASTM 3039 specimen geometries as applied previously. In axial testing, although the technique is the same for developing the equations, the assumptions are not the same. Figure 6 shows a representation of an axial tensile test, which was the basis for the axial constitutive equation development. In an axial tension test, the axial ( $0^\circ$ ) fibers are oriented to the direction of loading. This is represented by orienting the four subcells perpendicular to the direction of loading.

An important point to note for the discussion that follows is that the composite is once again assumed to be loaded in the “x-direction.” That means that in terms of the unit cell orientation, the axis orientation is switched  $90^\circ$  from the transverse loading case. In other words, what was considered to be the y-direction previously is now the x-direction, and vice versa. In axial tension testing, only one uniform stress assumption needs to be applied for the equation development here. Since the unit cell is being pulled in the x-direction, the effective force in the y-direction must be zero. The forces in the y-direction in each of the subcells are also assumed to be equal. This assumption can be expressed mathematically as follows:

$$N_y^A = N_y^B = N_y^C = N_y^D = 0 \quad (14)$$

The CLPT equations based on equation (5) will be expressed for the y-direction only for the case of an axial tension test. Note that the  $A_{ij}$  terms are not the same as they were for the transverse tension testing, as the angles for  $m$  and  $n$  have changed by  $90^\circ$  because the orientation of the unit cell has changed by  $90^\circ$ .

$$N_y^A = 0 = A_{12}^A * \epsilon_x^A + A_{22}^A * \epsilon_y^A \quad (15)$$

$$N_y^B = 0 = A_{12}^B * \epsilon_x^B + A_{22}^B * \epsilon_y^B \quad (16)$$

By taking into account the  $90^\circ$  change in angle in the  $A_{ij}$  terms, there are now seven equations (eqs. (4), (6) to (9), (15), and (16)) and only six variables ( $Q_{11}$ ,  $Q_{12}$ ,  $Q_{22}$ ,  $Q_{66}$ , and  $N_y^a$ ,  $N_y^b$  for the transverse tensile test). Now 6 out of the seven equations can be used for the solution, and the seventh equation can be used for verification.

Since the ultimate goal is to find the equivalent unidirectional ply level properties required for the material model, the  $Q$  terms need to be decomposed in terms of engineering constants. They can be decomposed as follows:

$$Q_{11} = \frac{E_{11}}{1 - \nu_{12} * \nu_{21}} \quad (17)$$

$$Q_{22} = \frac{E_{22}}{1 - \nu_{12} * \nu_{21}} \quad (18)$$

$$Q_{12} = \frac{\nu_{21} * E_{11}}{1 - \nu_{12} * \nu_{21}} \quad (19)$$

$$Q_{66} = G_{12} \quad (20)$$

In equations (17) to (20), the variables  $E_{11}$ ,  $E_{22}$ ,  $G_{12}$ ,  $\nu_{12}$  (axial Poisson's ratio) and  $\nu_{21}$  are unknown. Again, there are more unknowns than equations. The final equation comes from elasticity theory:

$$\frac{E_{11}}{\nu_{12}} = \frac{E_{22}}{\nu_{21}} \quad (21)$$

Knowing the  $Q_{ij}$  from above and using equations (17) to (21),  $E_{11}$ ,  $E_{22}$ ,  $G_{12}$ ,  $\nu_{12}$ , and  $\nu_{21}$  can be found. These values are effective unidirectional engineering properties of the composite ply at each integration point in the finite element model.

### Development of Failure Parameters

Ply level material properties are one portion of the input requirements for Material 58 in LS-DYNA. The other input requirement is the initial ply level unidirectional failure strengths for the composite. The initial failure criteria implemented within Material 58 are based on the Hashin (ref. 15) failure criteria and have the parameters specified in table 1 as input.

TABLE 1.—FAILURE VALUES NEEDED FOR  
FINITE ELEMENT MATERIAL MODEL

Parameter	Description
E11T	Strain at longitudinal tensile strength
E11C	Strain at longitudinal compressive strength
E22T	Strain at transverse tensile strength
E22C	Strain at transverse compressive strength
GMS	Strain at in-plane shear strength
XT	Longitudinal tensile strength
XC	Longitudinal compressive strength
YT	Transverse tensile strength
YC	Transverse compressive strength
SC	Shear strength

Failure values required for the finite element material model were determined based on the composite test data. Preliminary observations were made on the full-field strain data from the various axial and

transverse tensile and compressive tests that were conducted. The easiest parameters to observe are the axial tensile values. The axial fibers are assumed to carry the majority of the load during an axial tensile test. As a result, the assumption was made that in this test the braided composite is effectively acting as a unidirectional laminated composite, and therefore the axial tensile strength obtained during the test could be extrapolated to be the axial tensile strength of the equivalent unidirectional layer. The value  $E_{11T}$  can be found by observing the strain in an axial tensile specimen at failure, and  $X_T$  can be found by recording the ultimate tensile strength that occurs at the ultimate strain. Figure 7 shows a representative example of the stress-strain curve obtained from an axial tension test, along with the extrapolated failure values.

In compression, the full-field strain data shows that the composite behaves as homogenous material. Unlike in tensile tests, there are no areas of high and low strain, but rather a uniform strain field is present in the composite. Knowing this,  $E_{11C}$  can be found by observing the strain in an axial compression specimen at failure. The  $X_C$  can be found by recording the ultimate compressive strength that occurs at the ultimate compressive strain. Figure 8, left, shows the uniform strain field present in an axial compression specimen, as measured by the optical measurement system, and figure 8, right, shows the effective stress-strain curve, along with the extrapolated failure values.

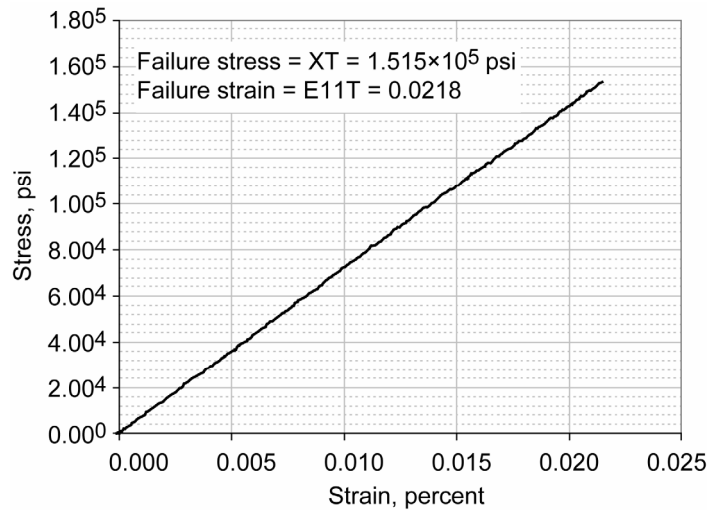


Figure 7.—Failure values gathered from an axial tension test.

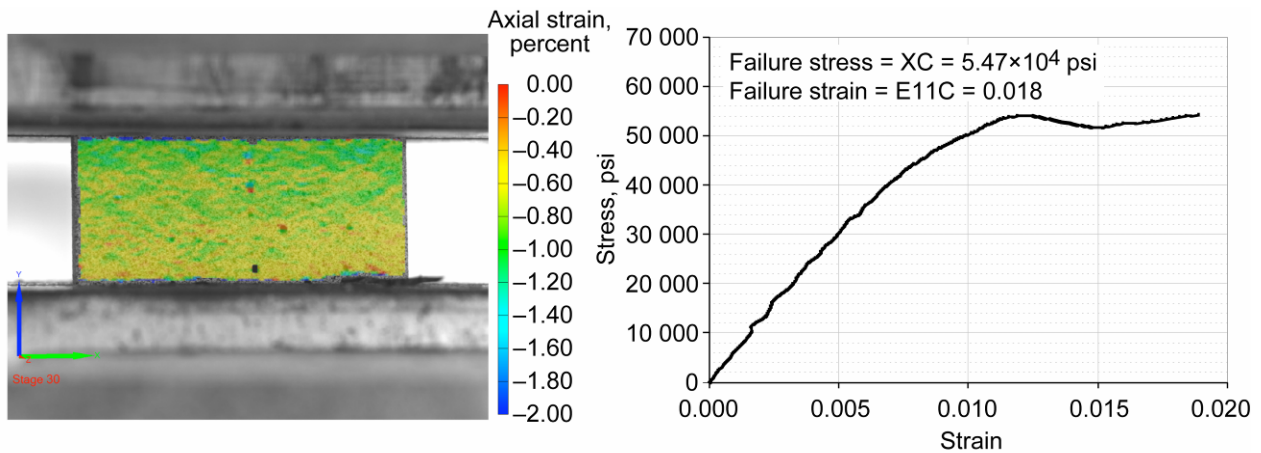


Figure 8.—Failure values gathered from an axial compression test.

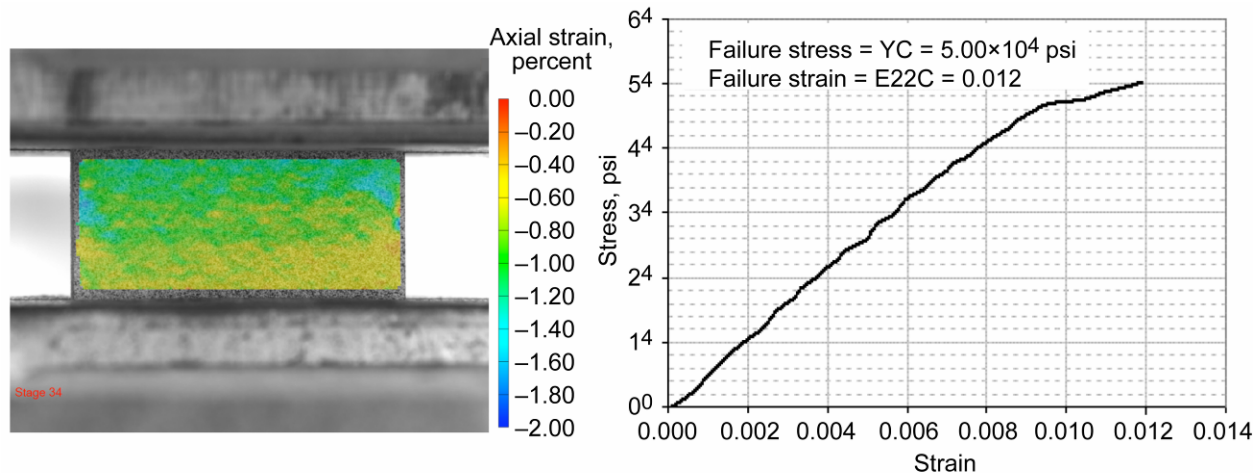


Figure 9.—Failure values gathered from a transverse compression test.

Similarly, for compression in the transverse direction, the composite also acts as a homogenous material. Both YC and E22C can be obtained from the material response in a transverse compression test. Figure 9, left, shows the uniform strain field present in a transverse compression specimen, and figure 9, right, shows the stress-strain response from a transverse compression test. Finding the tensile transverse failure values is not as straightforward. Since the failure strength input that is required is that of a unidirectional composite, the required transverse tensile strengths cannot be directly inferred by looking at the composite coupon stress-strain data because of the fact that the bias fibers significantly contribute to the composite failure strength. Instead a different approach was used to extrapolate the required values. By using the full-field strain measurement technique, the failure stress where the transverse fiber bundle split appears can be determined. This value is assumed to be YT. A detailed explanation on fiber bundle splitting can be found in reference 10. The fiber bundle split can be assumed to represent a transverse failure in each layer in the composite. However, the composite will fail once the overall composite material response reaches its failure strain, E22T. Between the onset of the splitting in the individual fiber bundles (YT) and specimen failure (E22T), damage is accumulating in the composite, which is demonstrated by the nonlinearities in the overall specimen stress-strain curve. As individual fiber bundles reach their failure stress and split, they cannot carry anymore load, and the load is distributed to the other fiber bundles. As the remaining fiber bundles begin to carry the extra load from the failed bundles, they, in turn, begin failing. When the number of fiber bundle failures reaches a critical value, the composite specimen will then fail.

The transverse failure caused by the fiber bundle splitting is represented in the model by setting the transverse tensile stress limiting parameter (SLIMIT2) equal to 1. Setting this parameter to 1 makes each individual layer for each of the subcells in the model behave in a simulated elastic-perfectly plastic manner in the transverse direction. In the elastic region, the fiber bundles are carrying load until they reach their ultimate stress value (YT). They then go into the plastic region. The plastic region represents the region in which each layer cannot carry any more load and simulates the loading on the layer after a fiber bundle split occurs in the composite test. It allows for the overall composite specimen to still carry load, even though individual fiber bundles cannot. This means that even though some of the individual fiber bundles will have failed, the overall specimen stress versus strain material response will continue to grow. In the transverse direction, the material response for a single layer would be as shown in figure 10.

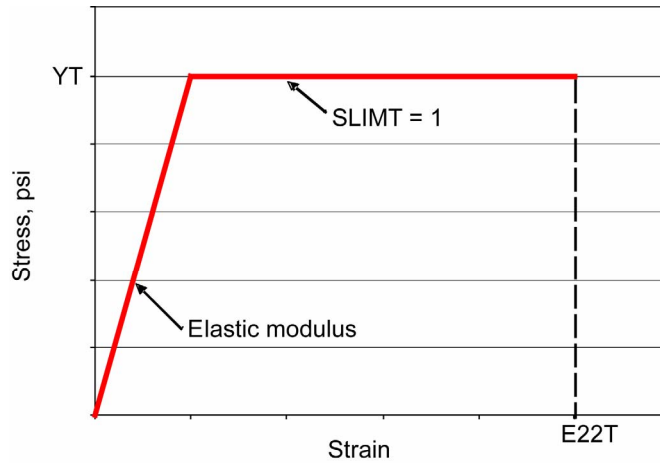


Figure 10.—Elastic plastic material response for a layer in the transverse direction.

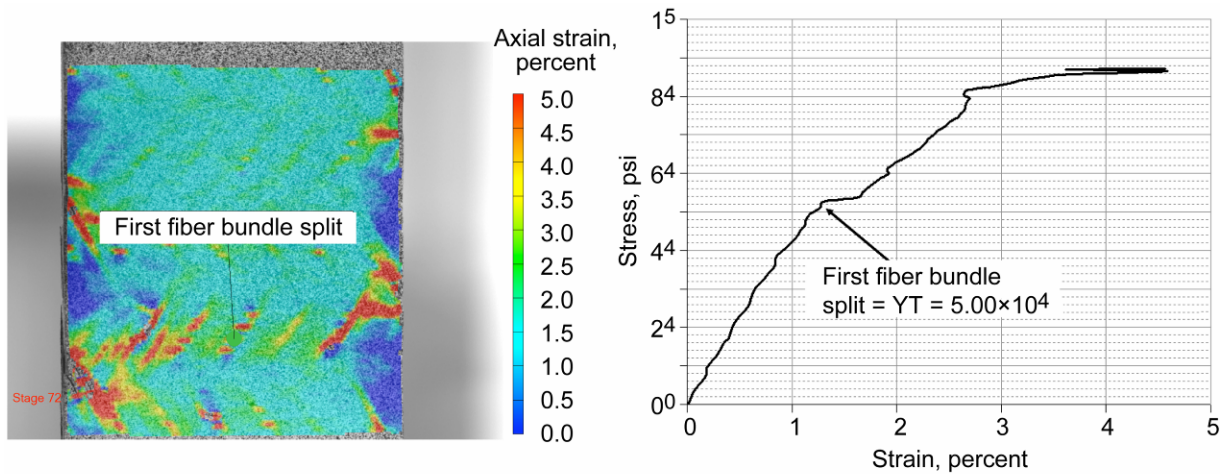


Figure 11.—Fiber bundle split view to obtain YT value.

Figure 11 shows the full-field strain measurement on a representative transverse tensile coupon and the local fiber bundle strain versus global coupon stress response obtained from a transverse tensile test, where the location of the first fiber bundle split is identified in the figure.

The value of E22T used in the analysis will be the strain at which the composite specimen fails. The value for E22T is taken from the overall composite stress-strain response. The overall composite transverse tensile stress versus strain response is shown in figure 12.

Shear strength parameters were found using the results from shear tests conducted according to ASTM D 5379 (ref. 14). Figure 13 shows the orientation of the unit cell under shear loading.

As figure 13 shows, each of the unit cells will take the same shear stress. If the thicknesses in each layer are assumed to be the same, then each layer for each unit cell will also take the same shear stress. Knowing this, the shear strength data measured from the test can be assumed to be equal to the equivalent unidirectional values. A representative shear stress versus strain response is shown in figure 14.

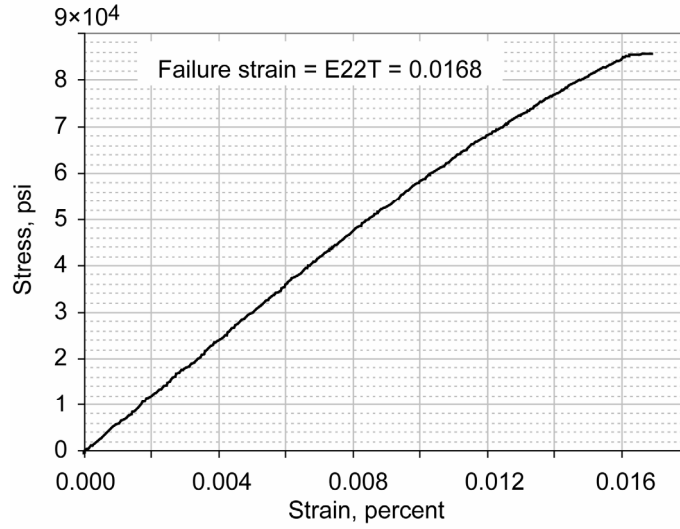


Figure 12.—Overall material response for E22T in a transverse tensile test.

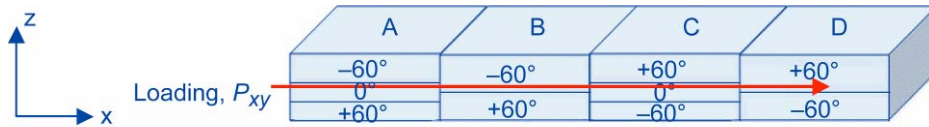


Figure 13.—Shear loading on the unit cell.

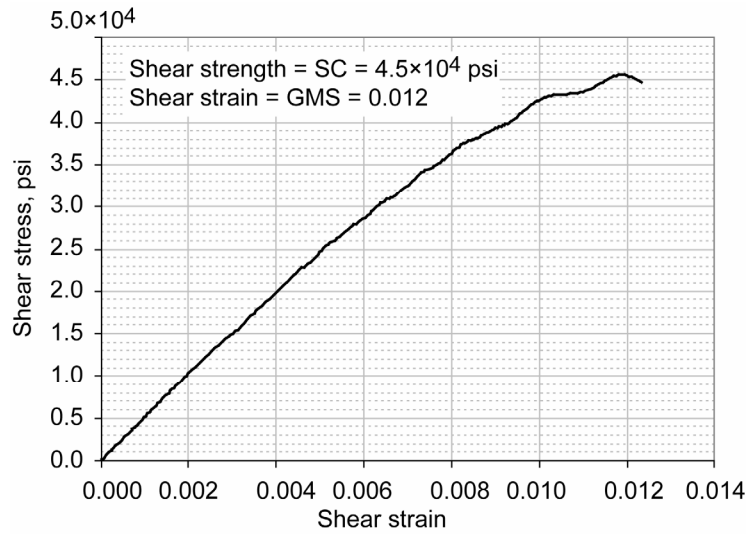


Figure 14.—Overall material response for a shear test.

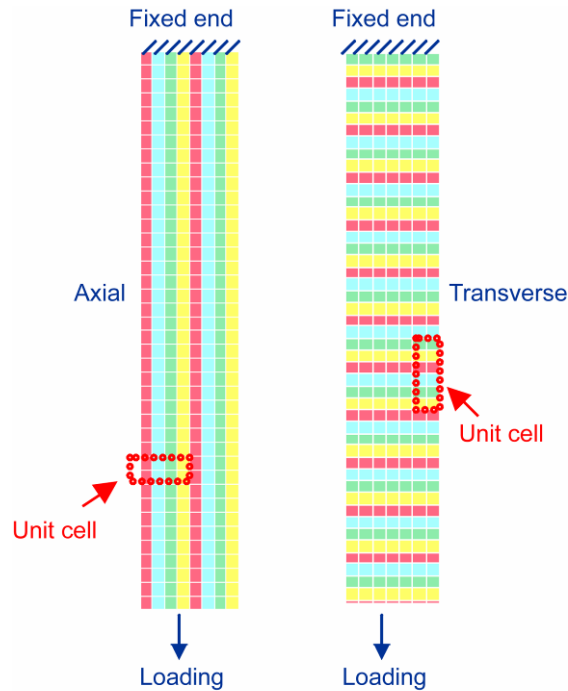


Figure 15.—Specimen geometries used in finite element model simulations.

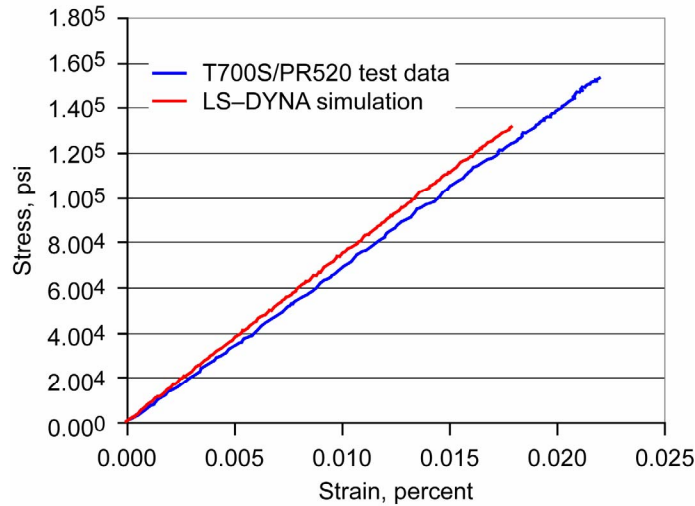


Figure 16.—Axial tensile stress comparison between representative test (blue) and finite element model (red) results.

### Finite Element Model Implementation

Two finite element models were created in LS-DYNA, one simulating an axial tensile test and the other simulating a transverse tensile test. Both geometries were based on ASTM 3039 geometries. Figure 15 shows the geometries.

Axial and transverse tensile tests were simulated in LS-DYNA, and the effective stress versus strain material response plots were output for each test. The stress-strain plots for the LS-DYNA simulations were compared against stress-strain curves obtained from the tests. Figure 16 shows the axial tension stress-strain curve obtained from a representative test and the equivalent stress-strain curve obtained from an LS-DYNA simulation.

TABLE 2.—COMPARISONS BETWEEN TEST AND LS-DYNA AXIAL TENSION DATA

	Axial tension modulus, psi	Axial tension strength, psi
Test	$6.8 \times 10^6 \pm 1.6 \times 10^5$	$1.52 \times 10^5 \pm 4.9 \times 10^3$
LS-DYNA	$7.4 \times 10^6$	$1.31 \times 10^5$
Error, percent	7	12

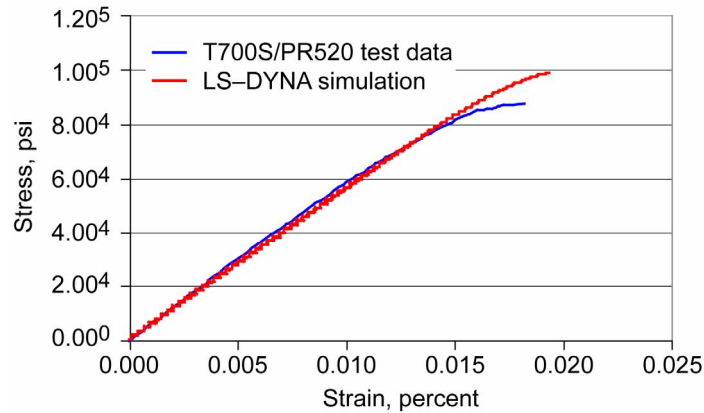


Figure 17.—Transverse tensile stress comparison between test (blue) and finite element model (red) results.

TABLE 3.—COMPARISONS BETWEEN TEST AND LS-DYNA TRANSVERSE TENSION DATA

	Transverse tension modulus, psi	Transverse tension strength, psi
Test	$6.2 \times 10^6 \pm 2.3 \times 10^5$	$8.69 \times 10^4 \pm 4.3 \times 10^2$
LS-DYNA	$5.6 \times 10^6$	$9.38 \times 10^4$
Error, percent	9	8

The preliminary comparisons between a sample axial test and LS-DYNA simulations show fairly good agreement. Table 2 compares the results between the LS-DYNA simulation and average test results. Note the numbers for the test data represent the average and one standard deviation for five tests.

The axial test results showed that the material modulus for the simulation agrees fairly well with the material modulus for the test; however, the strength obtained with the simulation is low compared with the test data. One reason for this discrepancy is that the value chosen for axial strength (XT) was from a statistical outlier generated from testing. Another reason is that the material used in LS-DYNA is represented by a continuum damage model. This means that damage could be occurring in the axial layers, leading to a reduced strength in these layers that does not actually occur in the test. Also, interactions between each layer could be causing localized stress concentrations in the LS-DYNA model that may not be present in the test. However, the model does show agreement with the test in that both response curves show linear behavior until failure.

Figure 17 shows transverse tensile stress-strain curves for a representative test and for an LS-DYNA simulation. The transverse results also show fairly good agreement between the test results and the simulation. Table 3 shows the comparisons.

The simulations capture the nonlinearities usually encountered with transverse testing due to damage accumulation in the composite. However, the strength values for the simulation were higher than the test. This could be due in part to the value picked for the transverse strength of the fiber bundle split. More

detailed investigations are needed to determine if the first fiber bundle split should be used for the analysis, or a median value of stress based on the number of fiber bundle splits should be used.

## Conclusions

A modeling technique has been developed for two-dimensional triaxial braided composites that characterizes the material response. This method uses a braided through the thickness integration approach to account for the fiber angles within a single unit cell and utilizes test data acquired from a full-field optical measurement system. The method combines assumptions from Classical Laminated Plate Theory and techniques derived from composite micromechanics approaches to create a method in which uniaxial ply level material properties entered into the finite element models come directly from measured test data on two-dimensional triaxial braids.

Further work can be done to examine the material response of two-dimensional triaxial braided composite materials under compression and shear loading. Appropriate finite element models, including proper boundary conditions, need to be developed for these simulations to be conducted.

## References

1. Christensen, J.M., *Mechanics of Composite Materials*. John Wiley and Sons. 1979.
2. Tan, P. et al., "Modeling for Predicting the Mechanical Properties of Textile Composites—A Review," *Composites Part A*, 28A. 1997.
3. Dano, M. et al., *Mechanical Behavior of Triaxial Woven Fabric Composite*. *Mechanics of Composite Materials and Structures*, 7. 2000.
4. Masters, John E. et al., *Mechanical properties of Triaxially Braided Composites: Experimental and Analytical results*. *Journal of Composites Technology & Research*, Vol. 15 No. 2. 1993.
5. Donadon, M.V. et al., *A 3-D Micromechanical Model for Predicting the Elastic Behaviour of Woven Laminates*. *Composite Science and Technology* 67. 2007.
6. Huang, Z.M., *A Unified Micromechanical for the Mechanical Properties of Two Constituent Composite Materials, Part I: Elastic Behavior*. *Journal of Thermoplastic Composite Materials* v13. 2000.
7. Ishikawa, T. and Chou T.W., *Elastic Behavior of woven hybrid composites*. *Journal of Composite Materials*, 16. 1982.
8. Tanov, R. and Tabiei, A., *Computationally Efficient Micromechanical Models for Woven Fabric Composite Elastic Moduli*. *Journal of Applied Mechanics*, 68. 2001.
9. LSTC. *LS-DYNA Users Manual v 971*. 2007.
10. Littell, J.D. et al., "Characterization of Triaxially Braided Composites Using Optical Measurement Techniques," *ASCE Earth and Space 2008 Conference Proceedings*.
11. Cheng, J., *Material Modeling of Strain Rate Dependent Polymer and 2D Tri-Axially Braided Composites*. University of Akron, Ph.D. dissertation, 2006.
12. Matzenmiller, A. et al., *A Constitutive Model for Anisotropic Damage in Fiber-Composites*. *Mechanics of Materials* 20, 125–152. 1995.
13. ASTM D 3039. *Standard Test Method for Tensile Properties of Polymer Matrix Composites*. 2000.
14. ASTM D 5379. *Standard Test Method for Shear Properties of Composite Materials by the V-Notched Beam Method*. 2005.
15. Hashin, Z., *Failure in Unidirectional Fiber Composites*. *Journal of Applied Mechanics* 47, 329. 1980.